Nanoscale

Accepted Manuscript

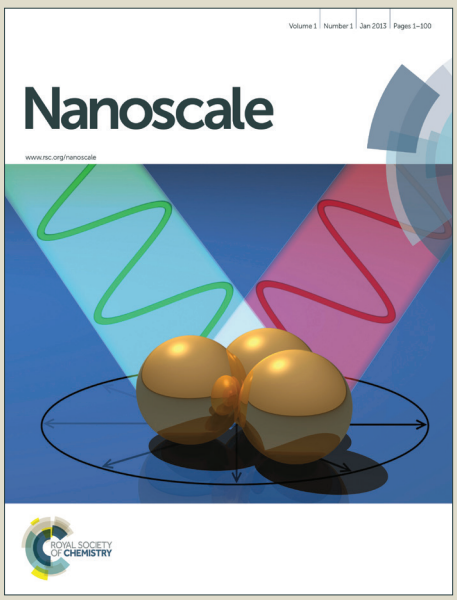

ROYAL SOCIETY OF CHEMISTRY

www.rsc.org/nanoscale

Journal Name

RSCPublishing

ARTICLE

$Li_{1.2}Mn_{0.6}Ni_{0.1}Co_{0.1}O_2$ Microspheres Constructed by Hierarchically Arranged Nanoparticles as Lithium Battery Cathode with Enhanced Electrochemical Performance

Cite this: DOI: 10.1039/x0xx00000x

Received 00th January 2012,
Accepted 00th January 2012

DOI: 10.1039/x0xx00000x

www.rsc.org/

P. Remith[a] and N. Kalaiselvi*[a]

Novel lithium rich layered $Li_{1.2}Mn_{0.6}Ni_{0.1}Co_{0.1}O_2$ microspheres containing hierarchically arranged and interconnected nanostructures have been synthesized by a combination of template free co-precipitation and solid state methods. The *in situ* formed γ-MnO_2 spherical template upon co-precipitation gets sacrificed during the course of solid state fusion of cobalt, nickel and lithium precursors to produce the title compound in the form of microspheres constructed by nanoparticles as building blocks. Porous and hollow microspheres of $Li_{1.2}Mn_{0.6}Ni_{0.1}Co_{0.1}O_2$ are formed out of the spontaneous aggregation of nanoparticles, obtained from the custom designed synthesis protocol. The growth mechanism of $Li_{1.2}Mn_{0.6}Ni_{0.1}Co_{0.1}O_2$ spheres could be understood in terms of Kirkendall effect and Ostwald ripening. The nanocrystalline $Li_{1.2}Mn_{0.6}Ni_{0.1}Co_{0.1}O_2$ compound is obtained as a solid solution consisting of rhombohedral $R\bar{3}m$ and monoclinic $C2/m$ group symmetries, as evidenced by XRD, Raman spectra and HRTEM equipped with FFT and STEM. The currently synthesized $Li_{1.2}Mn_{0.6}Ni_{0.1}Co_{0.1}O_2$ cathode exhibits an appreciable discharge capacity of 242 mAh g^{-1} at a current density of 50 mA g^{-1}, due to the synergistic effect of capacity obtained from rhombohedral and monoclinic phases.

1. Introduction

Rechargeable lithium-ion batteries, the energy efficient, green and zero emission batteries have attracted considerable attention of the researchers worldwide.[1] The high energy density, high operational voltage, high reversibility and long cycle life make them an excellent choice of power source for a wide variety of consumer market based e-gadgets than any other energy storage devices like lead-acid, nickel-cadmium and nickel-metal hydride batteries.[2-6] However, the energy density and cycle life of presently available lithium-ion batteries still need to be improved to meet with the multifarious requirements of the modern e-society. The low capacity (ca. 140 mA h g^{-1}), unreliable safety, high cost (of cobalt) and toxicity of $LiCoO_2$ provoke a pressing need to seek for alternative cathode candidates for use in high energy and power density applications. Here again, development of an alternative cathode, preferably with a layered structure to deliver high capacity poses numerous challenges. Further, it is well known that similar category single phase layered oxides such as $LiMnO_2$ and $LiNiO_2$ are found to suffer from unavoidable poor cycleability and rate capability issues. On the other hand, lithiated transition metal oxides could be tailored to obtain high capacity or high voltage cathodes by adjusting the metal to lithium ratio and/or by introducing an aliovalent dopant as in the case of three-component layered $LiNi_xMn_yCo_zO_2$ ($0 \le x,y,z < 1$) cathode that exhibits promising electrochemical properties.[7-9]

In recent years, $xLi_2MnO_3 \cdot (1-x)LiMO_2$ (M = Ni, Co, Mn) cathodes have been investigated as alternatives to the commercially exploited $LiCoO_2$ and other single phase cathodes in lithium-ion batteries.[10-13] In general, lithium rich layered $Li[M_{1-x}Li_x]O_2$ compounds exist as solid-solutions containing a rhombohedral $LiMO_2$ phase ($R\bar{3}m$ symmetry) and a monoclinic Li_2MnO_3 phase ($C2/m$ symmetry).[11,12] This unique framework of lithium rich layered compounds offers a

specific capacity as high as 250 mA h g^{-1}, compared with those of olivine (ca. 170 mA h g^{-1}) or spinel (ca. 130 mA h g^{-1}) cathode materials, to meet with the increasing demands of next generation energy storage applications. However, two major disadvantages, namely, low initial coulombic efficiency and poor rate capability associated with such lithium rich layered cathodes prohibit their practical application and wider acceptance in field trials. To mitigate the above mentioned problems, significant efforts have been made that include reduction of particle size, surface modification and adoption of morphology controlled synthesis of nanoarchitectures, with an ultimate aim of qualifying lithium rich layered transition metal oxides for potential application in rechargeable lithium batteries.[14-17]

Generally, electrochemical properties of cathode materials are influenced by phase purity, particle size and distribution of particles. Nanostructured electrode materials are known to accommodate the strains associated with the Li insertion/extraction in a better manner than the microstructured materials. The reduction of crystallite size results in shorter lithium ion diffusion pathway and faster lithium diffusion kinetics, which would enhance the cycling performance and rate capability. On the other hand, the inherent larger surface area associated with the nanostructured materials intensifies the surface reactions and increases the capacity fade, especially upon prolonged cycling.[18-24]

Hierarchically engineered micro/nanostructured metal oxide architectures find their application in wide range of fields, including catalysis, supercapacitor and water separation due to their unique structure-dependant physical and chemical properties.[25-28] Herein, the nanoparticles reduce the lithium ion diffusion pathway and the microstructure reduces the adverse effects of surface area related issues. It is well established that synthesis method plays a vital role in designing a compound with micro/nanostructure and qualifying the material to be active towards intercalation/de-intercalation of lithium ions. In this regard, the easy-to-adopt conventional solid state method requires high calcination temperature with longer duration of heating, whereas the soft chemistry approach involving sol-gel, co-precipitation and combustion methods requires utmost care to obtain homogenous distribution of particles with desired size and shape to exhibit good electrochemical performance. Templating is another approach to produce nanostructures with unique morphology and properties. Therefore, to synthesize a cathode material with desired morphology and good electrochemical performance, a hybrid methodology which will offer synergistic advantages of conventional solid state and soft chemical techniques including sacrificial templating approach has to be explored.

Herein, we designed a high capacity lithium rich layered $Li_{1.2}Mn_{0.6}Ni_{0.1}Co_{0.1}O_2$ cathode prepared in the form of porous microspheres constructed by hierarchically arranged nanoparticles by a self sacrificial template approach with γ-MnO_2 as the template. Interestingly, the compound is found to be a solid solution of $R\bar{3}m$ and *C2/m* space group symmetries. The Li_2MnO_3 component with *C2/m* symmetry not only enhances the stability of the orthorhombic $LiMO_2$ ($R\bar{3}m$) cathode structure, but also offers its due share of capacity, especially above 4.5 V region. As a result, the as-prepared $Li_{1.2}Mn_{0.6}Ni_{0.1}Co_{0.1}O_2$ cathode exhibits a high initial capacity of 242 mA h g^{-1} at a current density of 50 mA g^{-1}.

2. Experimental

2.1. Material Synthesis

The $MnCO_3$ microspheres were prepared by a template free co-precipitation method. Typically, stoichiometric amount of $MnSO_4 \cdot H_2O$ was dissolved in a mixture of H_2O and ethanol. 10% excess concentration of $NaHCO_3$ was dissolved in 500 mL of H_2O and poured into the $MnSO_4$ solution under vigorous stirring. The solution was stirred for 2 h and the product ($MnCO_3$ microspheres) was separated by centrifugation and dried at 120 °C for 12 h.

Porous γ-MnO_2 microspheres were obtained by a controlled thermal treatment at 500 °C for 2 h at a heating rate of 1 °C per minute. To obtain $Li_{1.2}Mn_{0.6}Ni_{0.1}Co_{0.1}O_2$ microspheres, required amount of $CoSO_4 \cdot 6H_2O$, $NiSO_4 \cdot 4H_2O$ and $LiOH \cdot H_2O$ along with γ-MnO_2 microspheres were mixed and ground well with the help of mortar and pestle. Then the powder was furnace heated at 800 °C for 8 h at a heating rate of 5 °C per minute.

2.2. Material Characterization

XRD analysis was carried out in Bruker D8 Advance X-ray diffractometer with non-monochromatic Cu Kα- radiation source and with a nickel monochromator for the diffracted beam. The XRD data was collected from 10 to 80 in 2θ at a scanning rate of 2 degree per minute. Unitcell lattice constants were calculated from the XRD data using "unitcell" software. Laser Raman microscopy was performed on a Renishaw 200 system with an argon ion laser and charge coupled device detector. FESEM images were captured using Zeiss Field Emission Scanning Electron Microscope. TEM studies were performed in Tecnai 20 G2 (FEI make) Transmission Electron Microscope, HRTEM investigations and STEM elemental mapping were performed using a JEOL JEM 2100 microscope operated at 200 kV. SAED patterns were marked with d spacing values using "Diffraction Ring Profiler" software. Nitrogen sorption analysis was carried out using a NOVA 3200e surface area and pore size analyzer. The pore size distribution plot was recorded based on the Barrett–Joyner–Halenda (BJH) model. Conductivity measurements were done using Wayne Kerr 6500 P high-frequency LCR meter. Powder samples were made into pellets of 2-3 mm thickness and 15 mm diameter and sintered further at 400 °C for 5h. Herein, the pellets were coated on both sides with a conducting silver paste and sandwiched between stainless steel blocking electrodes.

2.3. Electrochemical Studies

Electrodes were prepared by casting a mixture of 80 wt.% $Li_{1.2}Mn_{0.6}Ni_{0.1}Co_{0.1}O_2$, 10 wt.% super-P carbon and 10 wt.% PVdF binder suspended in N-Methyl-2-Pyrrolydone (NMP) solvent over aluminium foil. The coated electrode was dried under vacuum at 80 °C and subsequently heated to 120 °C overnight to evaporate the NMP solvent. CR2032 coin cells

supplied by Hohsen Corporation were used for the electrochemical measurements. Polypropylene membrane was used as the separator and 1M $LiPF_6$ dissolved in ethylene carbonate: diethylene carbonate (1:1 v/v) was used as the electrolyte. Cells were assembled in an argon filled glovebox (MBraun UNILAB). Charge/Discharge studies were carried out galvanostatically from 2.0 to 5.0 V with the help of ARBIN Charge/Discharge cycler. Cyclic voltammetry studies were performed on Biologic VSP electrochemical workstation in the voltage range 2.0- 5.0 V at a scan rate of 0.1 mV s^{-1}.

3. Results and Discussion

3.1. Synthesis of $Li_{1.2}Mn_{0.6}Ni_{0.1}Co_{0.1}O_2$ microspheres

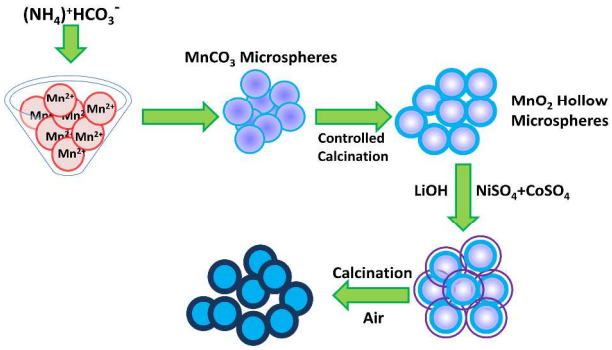

Scheme 1 Synthesis of $Li_{1.2}Mn_{0.6}Ni_{0.1}Co_{0.1}O_2$ using γ-MnO_2 microspheres as template.

Our approach to synthesize $Li_{1.2}Mn_{0.6}Ni_{0.1}Co_{0.1}O_2$ microspheres is illustrated in Scheme 1. The process is composed of two steps. The first step involves the production of hollow microspheres of γ-MnO_2 via. a simple co-precipitation method by using ammonium hydrogen carbonate as the precipitating agent. In the synthesis, an aqueous solution of manganese sulphate and NH_4HCO_3 are mixed together, and the resulting precipitate is stirred for about 1 h to ensure complete precipitation. When the reactants are mixed together, nanocrystalline $MnCO_3$ particles are obtained through co-precipitation. Upon controlled calcination, the *in situ* formed $MnCO_3$ particles aggregate spontaneously to form γ-MnO_2 hollow microspheres.[27] Herein, the ammonium sulphate directed crystallisation of $MnCO_3$ resulted in spherical morphology in the ethanol-water mixed solvent.[28] The as-obtained light purple coloured $MnCO_3$ microspheres are dried and furnace calcined under controlled heating conditions (2 $^{\circ}$C per minute) in open air to produce fine powders of γ-MnO_2 microspheres by the elimination of CO_2. The resulting porous and hollow microspheres of γ-MnO_2 microspheres, when mixed with LiOH, $CoSO_4$ and $NiSO_4$ and calcined further at 800 $^{\circ}$C for 10 h in air resulted in the formation of desired $Li_{1.2}Mn_{0.6}Ni_{0.1}Co_{0.1}O_2$ microspheres. During the calcination process, fast outward diffusion of Mn, Co and Ni atoms and slow inward diffusion of oxygen atoms take place to form a hollow microsphere structure, as explained by Kirkendall effect and Ostwald ripening.[29-31] The same has been discussed in detail with the images obtained from TEM analysis.

3.2. Morphology Studies

The morphology of hierarchically arranged nanoparticles of $Li_{1.2}Mn_{0.6}Ni_{0.1}Co_{0.1}O_2$ to form the hollow microsphere was characterized by field emission scanning electron microscopy (FESEM). Fig. 1 shows the FESEM images of $MnCO_3$ (Fig. 1a-c) and γ-MnO_2 microspheres (Fig. 1d-f), evidencing the uniformly dispersed microspheres with a diameter ranging from 2 to 3 µm. FESEM further confirms the presence of uniformly formed microstructures with spherical morphology (Fig. 1d and e). Finer crystals of γ-MnO_2 microspheres are composed of narrowly distributed nanoparticles with triangular edges and corners (Fig. 1f), as reported by Jinbo Fei *et.al*.[28]

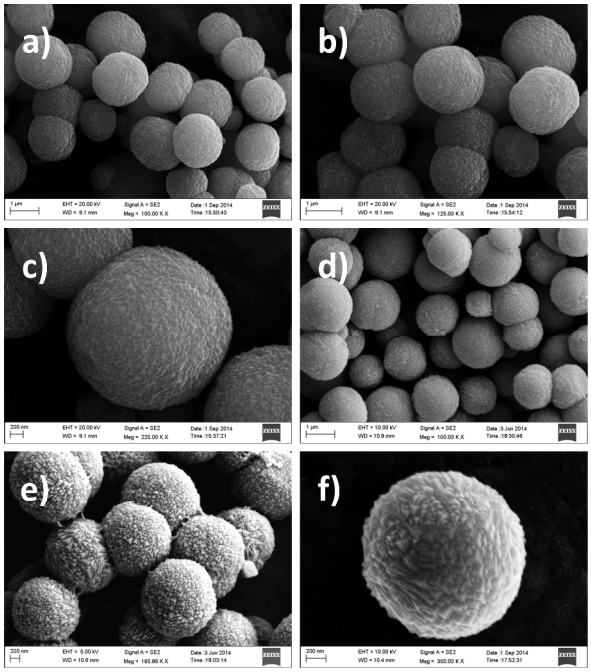

Fig. 1 (a, b and c) FESEM images of $MnCO_3$ microspheres (d, e and f) FESEM images of *in situ* formed γ-MnO_2 template possessing triangular edges and corners.

Fig. 2 shows the FESEM images of pristine $Li_{1.2}Mn_{0.6}Ni_{0.1}Co_{0.1}O_2$, evolved from γ-MnO_2 microspheres. The low magnification images (Fig. 2a and b) show that the size of $Li_{1.2}Mn_{0.6}Ni_{0.1}Co_{0.1}O_2$ microspheres typically ranges from 5 to 6 µm. Further, it is evident from Fig. 2b and c that the micrometer-sized spherical particles are composed of hierarchically arranged nanoparticles. The surface of the microspheres indicates the presence of irregularly shaped nanoparticles (Fig. 2d) arranged in such a manner to form a porous surface, which in turn is expected to facilitate enhanced electrolyte penetration and lithium ion diffusion from/to the electrode. The closer view of a microsphere in Fig. 2c clearly shows that the primary particles are present in the nano regime with a size ranging from 50 to 70 nm. Fig. 2e and f clearly

confirm that the $Li_{1.2}Mn_{0.6}Ni_{0.1}Co_{0.1}O_2$ compound has been synthesized in the form of hollow microsphere.

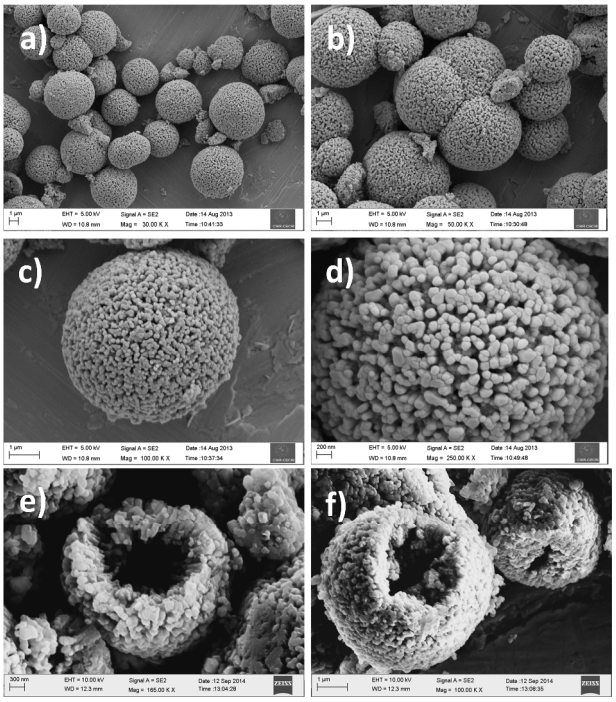

Fig. 2 (a and b) Low magnification FESEM images of $Li_{1.2}Mn_{0.6}Ni_{0.1}Co_{0.1}O_2$ microspheres obtained at 800 ^oC (c and d) High magnification images showing the aggregation of nanoparticles to form microspheres (e and f) High magnification images indicating the hollow interior of $Li_{1.2}Mn_{0.6}Ni_{0.1}Co_{0.1}O_2$ spheres.

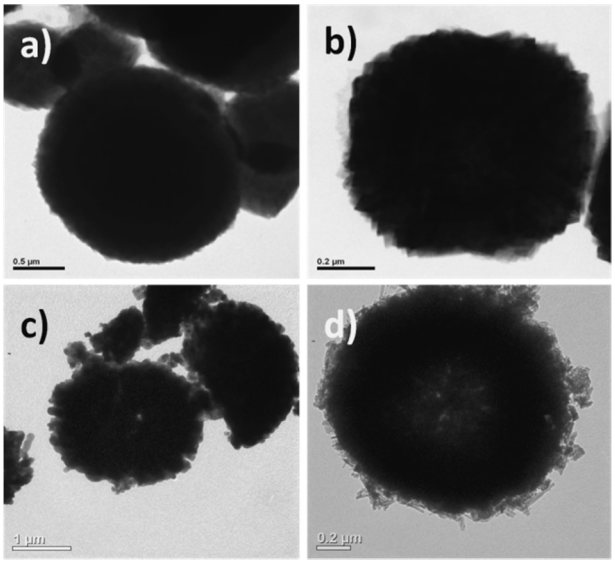

Fig. 3 (a and b) TEM images of γ-MnO_2 solid microspheres possessing sharp edges on the surface (c and d) TEM images of $Li_{1.2}Mn_{0.6}Ni_{0.1}Co_{0.1}O_2$ microspheres evidencing the presence of hollow interior.

TEM images provide more information on the formation mechanism viz., microscale Kirkendall effect, which is believed to be responsible for the formation of the hollow microspheres of the final compound. Fig. 3 shows the typical bright-field TEM images of γ-MnO_2 (Fig. 3a and b) and $Li_{1.2}Mn_{0.6}Ni_{0.1}Co_{0.1}O_2$ microspheres (Fig. 3c and d). The solid or dense microspheres of γ-MnO_2 (Fig 3a and b) upon furnace calcination led to the formation of hollow $Li_{1.2}Mn_{0.6}Ni_{0.1}Co_{0.1}O_2$ microspheres, with an average wall thickness of 350 nm. The brighter contrast at the centre of Fig. 3c and d confirms that the final product viz., $Li_{1.2}Mn_{0.6}Ni_{0.1}Co_{0.1}O_2$ is having a hollow interior, which is in accordance with the FESEM results. The hollow spheres of the final product and the solid spheres of the precursor confirm the fact that the formation mechanism involved in the present case is the microscale Kirkendall effect in preparing the hollow microspheres of $Li_{1.2}Mn_{0.6}Ni_{0.1}Co_{0.1}O_2$ using co-precipitation and solid state methods. In other words, the precursor that contains a mixture of cobalt, lithium and nickel salts forms the desired compound with a hollow structure, due to the difference in the diffusion rate of various metal and oxygen atoms. The same has been evidenced by TEM results, which is quite interesting.

The porous structure of $Li_{1.2}Mn_{0.6}Ni_{0.1}Co_{0.1}O_2$ compound has been investigated by nitrogen sorption studies. The Brunauer−Emmett−Teller (BET) surface area measurement and pore size distribution of $Li_{1.2}Mn_{0.6}Ni_{0.1}Co_{0.1}O_2$ microspheres are shown in Fig. 4. The BET surface area is 13.8 m^2g^{-1} and the microspheres are found to contain mesoporous structure, according to the Barrett-Joyner-Halenda (BJH) plot.

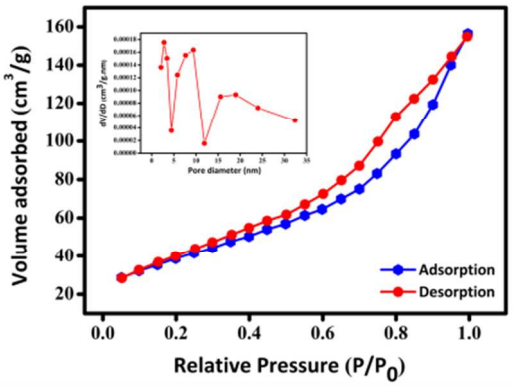

Fig. 4 Nitrogen sorption isotherm of $Li_{1.2}Mn_{0.6}Ni_{0.1}Co_{0.1}O_2$ microspheres (Inset: Barrett-Joyner-Halenda (BJH) pore size distribution plot).

3.3. X-Ray Diffraction and High Resolution Transmission Electron Microscopy Studies

The phase purity of $Li_{1.2}Mn_{0.6}Ni_{0.1}Co_{0.1}O_2$ has been confirmed by X-ray diffraction analysis (Fig. 5). The X-ray diffraction (XRD) pattern of the as-synthesized $MnCO_3$ microsphere is shown in Fig. 5a, which can be indexed to the pure rhombohedral lattice system of $MnCO_3$ (JCPDS Card Number

83-1763) with lattice parameter values such as a= 0.4784 nm, c= 1.5599 nm and the cell volume V= 309.2548 nm^3.[32] Sherrer formula derived lattice spacing value of d= 48.91 nm shows that the average crystallite size is in the nanometer range, as explained by FESEM results. Fig. 5b shows the XRD reflections of pristine MnO_2, which is characteristic of hexagonal γ-MnO_2 (JCPDS Card Number 78-390).[27] The broader peaks indicate the nanocrystalline nature of the as formed γ-MnO_2. It is worth mentioning that a complete transformation of $MnCO_3$ to MnO_2 has taken place, as evident from the absence of peaks due to $MnCO_3$ in the XRD pattern (Fig. 5b).

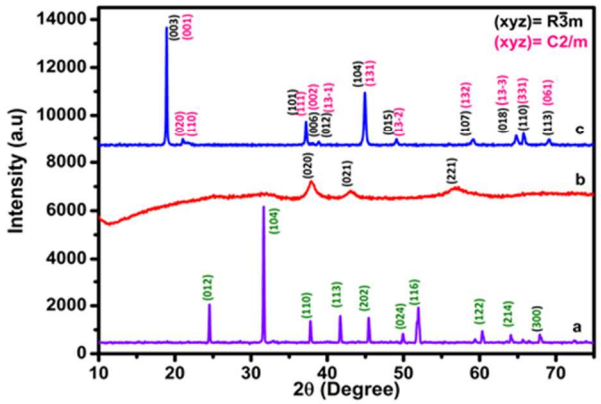

Fig. 5 XRD pattern of (a) as-prepared $MnCO_3$ precursor (b) *In situ* formed γ-MnO_2 microsphere template prepared by the thermal decomposition at 400 °C and (c) pristine $Li_{1.2}Mn_{0.6}Ni_{0.1}Co_{0.1}O_2$ microspheres prepared at 800 °C.

The XRD pattern of the as-synthesized cathode material (Fig. 5c) matches well with the $R\bar{3}m$ space group of rhombohedral α-$NaFeO_2$ structure, as reported by Xuan Zhao *et.al*.[33] The calculated lattice constants corresponding to $R\bar{3}m$ space group are a= 0.28 nm and c= 1.417 nm, which are in good agreement with the reported behavior. Particularly, the material is well-crystallized and no impurities are detected. The R value (I_{003}/I_{104}) is calculated to be 2.2, which is an indication of insignificant cation mixing and the peak splitting of (006)/(104) and (018)/(110) indicates perfect hexagonal arrangement of layered type of compounds.[34] Additionally, the two weak superlattice reflections located in the 2θ range from 20–25 degree are characteristic of Li_2MnO_3-based compounds with *C2/m* space group. Hence, it is understood that the currently prepared $Li_{1.2}Mn_{0.6}Ni_{0.1}Co_{0.1}O_2$ possesses a combination of two phases, namely rhombohedral $R\bar{3}m$ and monoclinic *C2/m*, due to which all the peaks could be indexed on the basis of $R\bar{3}m$ and *C2/m* symmetries. The XRD reflections and lattice constant values are analogous to the values reported for a similar compound by Karalee A. Jarvis *et. al*. and confirming that the compound is a solid solution between $R\bar{3}m$ and *C2/m* space group symmetries, which is noteworthy.[35-37] In other words, the title compound that exists as a solid solution corresponding to two different symmetries may be considered as a hybrid electrode material to exhibit synergistically advantageous properties, which is the highlight of the study.

High-resolution transmission electron microscopy (HRTEM) equipped with Fast Fourier transformation (FFT) and Scanning Transmission Electron Microscope (STEM) based elemental mapping has been used to examine the solid solution nature of the as synthesized compound. Further, as shown in Fig. 6a, the individual particles are found to get distributed in the narrow range of 50 to 80 nm with an average particle size of 70 nm. Closer view of a selected area is shown in Fig. 6b and c, which clearly depicts the existence of monoclinic arrangement of atoms in *C2/m* phase. This is also supported by the corresponding FFT image, shown as the inset of Fig. 6c. On the other hand, a magnified view of Fig. 6d- f displays the layered arrangement of atoms corresponding to $R\bar{3}m$ symmetry, which is further confirmed by the corresponding FFT image, shown as the inset of Fig. 6f. The lattice fringe spacing has been calculated as 4.7 Å, which perfectly matches well with the value obtained from XRD results. Consequently, one can conclude that the newly identified $Li_{1.2}Mn_{0.6}Ni_{0.1}Co_{0.1}O_2$ compound is a solid solution of *C2/m* and $R\bar{3}m$ symmetries.

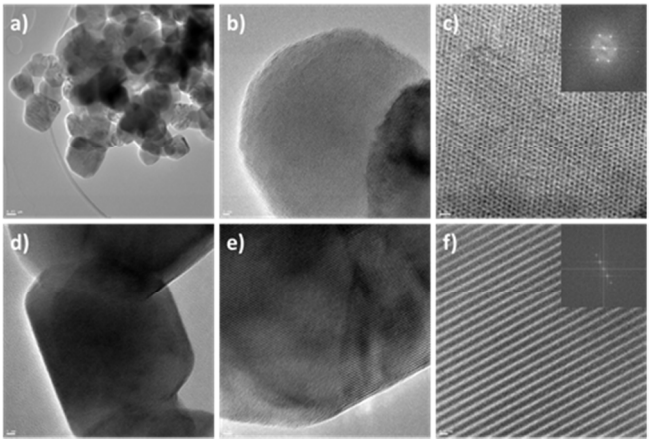

Fig. 6 HRTEM images of $Li_{1.2}Mn_{0.6}Ni_{0.1}Co_{0.1}O_2$ solid solution showing the presence of two phases, containing rhombohedral $R\bar{3}m$ and monoclinic *C2/m* symmetries, Insets are the corresponding digitalized Fast Fourier Transformed images of Fig. 6c and f.

STEM elemental mapping was done in order to obtain detailed information about the composition and the distribution of elements throughout the structure († Electronic Supplementary Information (ESI), Fig. S1). Fig. S1 shows the cumulative and individual elemental mapping (ESI Fig. S1a-e) of $Li_{1.2}Mn_{0.6}Ni_{0.1}Co_{0.1}O_2$ compound, which shows the presence of uniform distribution of respective elements viz., O, Mn, Ni and Co. Further, the stoichiometry of the currently synthesized $Li_{1.2}Mn_{0.6}Ni_{0.1}Co_{0.1}O_2$ compound has been verified using Energy Dispersive X-ray (EDX) spectrum († ESI, Fig. S2) and the percentage composition of different elements derived from the same has been furnished in ESI Fig. S1f.

We acquired selected area electron diffraction (SAED) pattern to probe the local structure († ESI, Fig. S3). Fig. S3 corresponds to the hexagonal diffraction pattern, wherein no peaks

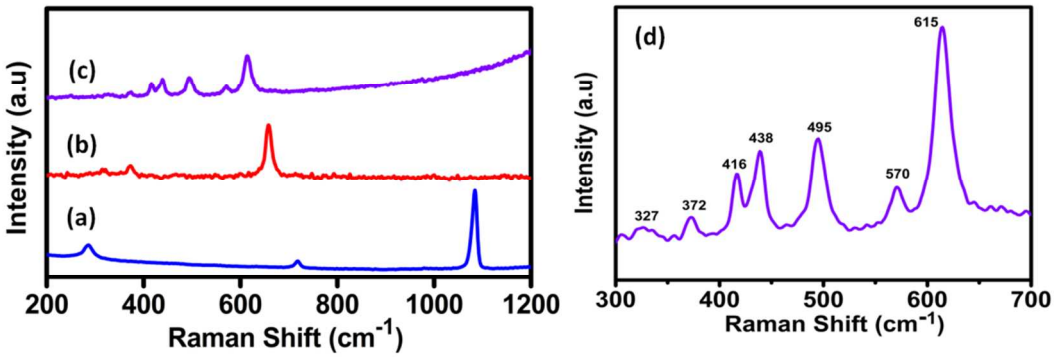

Fig. 7 Raman spectra of (a) $MnCO_3$, (b) γ-MnO_2 (c) Pristine $Li_{1.2}Mn_{0.6}Ni_{0.1}Co_{0.1}O_2$ and (d) Enlarged view of $Li_{1.2}Mn_{0.6}Ni_{0.1}Co_{0.1}O_2$

due to secondary phase impurities are seen. The points relevant to hexagonal phase could be indexed to the $R\bar{3}m$ space group symmetry. Furthermore, it is quite interesting to note that in the same SAED pattern, we are able to index (020) plane of *C2/m* space group, corresponding to the d spacing value of 1.29 nm († ESI, Table 1). Further, it is interesting to note that a striking similarity has been observed with the d-spacing values, derived from the (hkl) plane of XRD and TEM fringes. As a result, with the collective inference from XRD, HRTEM and SAED pattern, we are able to conclude that the title compound is a solid solution of $R\bar{3}m$ and *C2/m* space group symmetries.

3.4. Raman Spectroscopy and Conductivity Studies

Raman spectroscopy was used to study the local structure of the precursor as well as the final product by lattice vibrations. In Fig. 7a, three peaks situated at 1082, 761 and 285 cm^{-1} confirms the presence of rhodochrosite phase of $MnCO_3$. The sharp peak located around 650-700 cm^{-1} in Fig. 7b corresponds to the Mn-O bond in MnO_6 octahedra. Fig. 7c shows the Raman spectrum of pristine $Li_{1.2}Mn_{0.6}Ni_{0.1}Co_{0.1}O_2$, which displays several peaks around 300-700 cm^{-1}. Fig. 7d is the enlarged view of Fig. 7c, wherein peaks at 495 and 615 cm^{-1} are assigned to the Raman active E_g and A_{1g} symmetric stretching modes of metal-oxygen bonds in the rhombohedra. The low frequency bands are associated with the lithium-oxygen bonds. The shoulder peak at 570 cm^{-1} indicates an atomic arrangement, which can be assigned to the monoclinic *C2/m* phase, where the Mn atoms are bonded to the equatorial oxygen atoms.[38,39] Hence, it is substantiated from Raman studies that the monoclinic (*C2/m*) and rhombohedral ($R\bar{3}m$) phases co-exist in the currently synthesized $Li_{1.2}Mn_{0.6}Ni_{0.1}Co_{0.1}O_2$ solid solution.

Despite the interesting and encouraging morphological and structural properties of $Li_{1.2}Mn_{0.6}Ni_{0.1}Co_{0.1}O_2$, conductivity studies were carried out with a view to recommend the same for a possible electrochemical characterization and to demonstrate its application in rechargeable lithium batteries involving the intercalation and de-intercalation of lithium ions. Conductivity measurements at different temperatures show a typical graph (Fig. 8), characteristic of oxide ceramic materials. The inset in Fig. 8 shows the corresponding Arrhenius plot. The sample shows a linear dependence against inverse of temperature. The pristine sample shows a bulk conductivity of 1.58 μS m^{-1} at room temperature († ESI, Fig. S4) and the activation energy is calculated to be 0.35 eV. Further, the conductivity increases significantly beyond 300 ^{o}C. It is well known that mixed metal oxides possessing the same element in different oxidation states might show high conductivity due to hopping mechanism.[38] Accordingly, with an increasing temperature, conductivity of $Li_{1.2}Mn_{0.6}Ni_{0.1}Co_{0.1}O_2$ compound reaches 1.2 mS m^{-1}, which may be attributed to the occurrence of Mn^{3+}/Mn^{4+} in the neighbouring octahedral sites. Based on these grounds, enhanced lithium transport kinetics is anticipated, which in turn would improve the lithium storage capability and the cycle life behavior of title cathode in rechargeable lithium cell assembly.

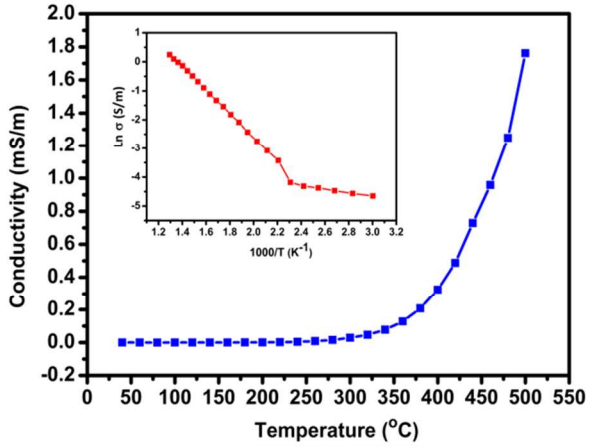

Fig. 8 Temperature dependant conductivity plot of pristine $Li_{1.2}Mn_{0.6}Ni_{0.1}Co_{0.1}O_2$ and the Inset shows the corresponding Arrhenius plot.

3.5. Electrochemical Lithium-Storage Performance

Fig. 9a exhibits the cyclic voltammetry (CV) plots of the $Li_{1.2}Mn_{0.6}Ni_{0.1}Co_{0.1}O_2$ microsphere cathode between 2.0 to 5.0 V, recorded at a scan rate of 0.1 mV s^{-1}. As seen from Fig. 9a,

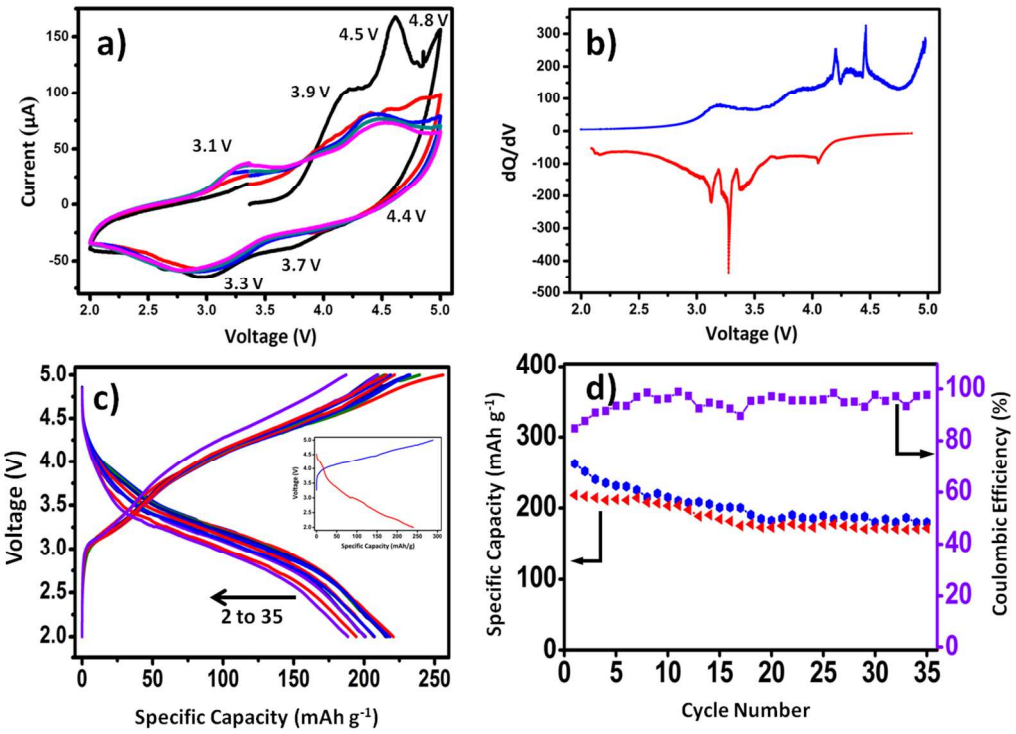

Fig. 9 (a) Cyclic Voltammogram of pristine $Li_{1.2}Mn_{0.6}Ni_{0.1}Co_{0.1}O_2$ cathode recorded at a scan rate of 0.1 mV s^{-1} (b) dQ/dV profile of the second cycle (c) Galvanostatic charge/discharge curves (Inset: First cycle charge-discharge capacity of $Li_{1.2}Mn_{0.6}Ni_{0.1}Co_{0.1}O_2$ cathode) and (d) Specific capacity and coulombic efficiency of $Li_{1.2}Mn_{0.6}Ni_{0.1}Co_{0.1}O_2$ cathode upon progressive cycling.

first cycle CV is entirely different from the remaining cycles and exhibiting two peaks at 3.9 and 4.8 V, which are due to the Mn^{3+} to Mn^{4+} and Ni^{2+} to Ni^{4+} redox couples respectively. The third peak at 4.5 V is due to the oxygen removal from the lattice as reported by M. M. Thackarey *et. al.*[11,41] As a result, some of the cobalt ions also get oxidised at the high voltage region. In the reverse scan, there are three peaks, of which peaks centered at 4.4 and 3.7 V are ascribed to the reduction of Ni^{4+} to Ni^{2+}. The peak at 3.3 V can be assigned to the reduction of Mn^{4+}. As can be observed from the cyclic voltammetry (Fig. 9a), the CV behavior of consecutive cycles is different from the first formation cycle, which may be understood as follows: During the initial and SEI formation cycle, fast elimination of oxide ion vacancies becomes unavoidable and uncontrollable, which is not unusual.[41,42] Nevertheless, upon progressive cycling, part of the oxide ion vacancies are retained, leading to the liberation of reduced number of oxygen ion vacancies and hence the subsequently addressed irreversible capacity loss related issue could be understood. The oxidation peak found at 3.9 V of the subsequent cycles is predominantly associated with the oxidation of Ni^{2+} to Ni^{4+}. In short, the electrochemical activation of Li_2MnO_3 to MnO_2 occurs at a potential as high as 4.4 V, which leads to the removal of oxygen from the lattice and resulting in an unavoidable irreversible capacity loss. Therefore, inferior coulombic efficiency would be obtained for the first cycle, which is quite reasonable. On the other hand, the high intense peak in the first cycle corresponding to the oxygen removal is found to be absent in the subsequent cycles, which is an exciting and supporting observation. Similarly, yet another remarkable observation is that the reverse scan still exhibits a peak at 3.3 V, which shows the involvement of Li_2MnO_3 regions in the redox reaction. The cathodic sweep has a peak below 3 V, which may be due to the transformation of layered to spinel structure. Although, cyclic voltammetry has provided the redox voltage of the cathode deployed in the freshly fabricated cell, exact reaction voltages could be clearly seen when dQ/dV curves are plotted against voltage (Fig. 9b). A small peak at 3.1 V and the sharp peaks above 4.2 V during charging are due to the Mn^{3+}/Mn^{4+} redox couple. The development of the 3 V plateau may be due to the unavoidable initial transformation of layered to spinel structure, which is characteristic of $LiMnO_2$ cathode.[43,44] In particular, the peak at 4.4 V is due to the activation of monoclinic Li_2MnO_3 region, which in turn offers its contribution to improve the capacity of $Li_{1.2}Mn_{0.6}Ni_{0.1}Co_{0.1}O_2$ cathode. Even though the discharge profile shows a sloping behavior, the dQ/dV curve displays a two step reaction, according to the possible redox pair formation discussed under CV studies.

The electrochemical performance of $Li_{1.2}Mn_{0.6}Ni_{0.1}Co_{0.1}O_2$ cathode has been investigated by charge/discharge studies. Fig. 9c displays the galvanostatic charge/discharge voltage vs. specific capacity profile. The cathode delivers an initial

discharge capacity of 242 mA h g^{-1} at a current density of 50 mA g^{-1} (Inset in Fig. 9c). Fig. 9d displays the charge/discharge capacity *vs.* cycle number and the corresponding coulombic efficiency values. The initial coulombic efficiency of $Li_{1.2}Mn_{0.6}Ni_{0.1}Co_{0.1}O_2$ cathode is 84%, which is far higher than the reported values and the initial irreversible capacity loss is only 46 mA h g^{-1}. Hence, the preparation of lithium rich layered oxide as cathode to offset the initial irreversible capacity loss (driven by the spontaneous removal of oxide ion vacancies upon initial discharge) has been achieved by preventing such elimination through the carefully designed structural arrangement of $Li_{1.2}Mn_{0.6}Ni_{0.1}Co_{0.1}O_2$ compound, bestowed with the synergistic benefits of microspheres and nanoparticles. More interestingly, the coulombic efficiency of $Li_{1.2}Mn_{0.6}Ni_{0.1}Co_{0.1}O_2$ after the first cycle is found to increase gradually and reaches above 95%, which is the significance of the study (Fig. 9d). In other words, it is the faster lithium ion diffusion facilitated by the hierarchically arranged nanoparticles of the microstructures with spherical morphology, wherein the hollow microspheres by way of permitting the easy percolation of electrolyte and the lithium rich composition by restricting the initial loss of oxide ion vacancies enhance the coulombic efficiency to the extent of 97%. As we discussed earlier, morphology and particle size are the key factors that are found to play a vital role in improving the lithium ion diffusion efficiency. The nanoparticles typically enhance the lithium ion diffusion, thereby increasing the lithium storage performance of $Li_{1.2}Mn_{0.6}Ni_{0.1}Co_{0.1}O_2$ cathode. Moreover, the partial removal of oxide ions from the lattice and the resulting activation of Li_2MnO_3 regions generate much higher capacities, which is noteworthy.

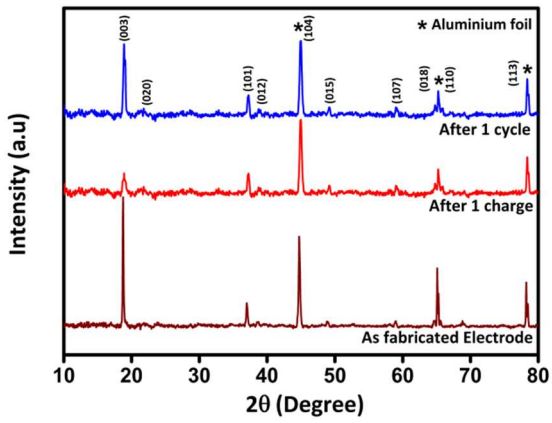

Fig. 10 *Ex situ* XRD pattern of $Li_{1.2}Mn_{0.6}Ni_{0.1}Co_{0.1}O_2$ (fresh electrode) and the corresponding diffractogram obtained after one charge and one cycle, wherein recurrence of (003) peak after completing one cycle evidences the stability and structural integrity of the title cathode.

Further, $Li_{1.2}Mn_{0.6}Ni_{0.1}Co_{0.1}O_2$ cathode of the present study delivers a steady state discharge capacity of 180 mA h g^{-1} upto 35 cycles, which is much better than the commercial $LiMn_{1/3}Ni_{1/3}Co_{1/3}O_2$ cathode that exhibits a discharge capacity of 144 mAh g^{-1} at the end of the 20th cycle († ESI, Fig. S6). In addition, with a view to understand and to demonstrate the cycling stability and structural integrity of crystalline $Li_{1.2}Mn_{0.6}Ni_{0.1}Co_{0.1}O_2$ microsphere cathode, *ex situ* XRD analysis has been carried out for the coated electrodes under three different conditions viz., as fabricated electrode, electrode after completing one charge and after the completion of one cycle. The results obtained are displayed in Fig.10. From the figure, it is evident that the intensity of the (003) peak reduces upon de-lithiation (charge) and gets resumed upon subsequent discharge process (*i.e.*, after the completion of one cycle), thus qualifying the same for progressive cycling. Hence, the cycling stability of the layered $Li_{1.2}Mn_{0.6}Ni_{0.1}Co_{0.1}O_2$ cathode and the integrity of the crystalline structure upon cycling are better understood from the said behavior, thus enabling to recommend the $Li_{1.2}Mn_{0.6}Ni_{0.1}Co_{0.1}O_2$ cathode as yet another potential candidate for use in rechargeable lithium batteries.

4. Conclusions

In conclusion, we have successfully prepared novel lithium rich layered $Li_{1.2}Mn_{0.6}Ni_{0.1}Co_{0.1}O_2$ microspheres, formed out of hierarchically arranged and interconnected nanocrystalline particles by a simple co-precipitation method followed by conventional solid state approach. The formation mechanism of the obtained structure could be understood in terms of self transforming Ostwald ripening and Kirkendall effect. The results of physical characterization confirm the fact that the spherical structure of the $MnCO_3$ precursor has been preserved in the final $Li_{1.2}Mn_{0.6}Ni_{0.1}Co_{0.1}O_2$ compound, mediated through spherical γ-MnO_2 template, as confirmed by FESEM. The porous and hollow microstructure of $Li_{1.2}Mn_{0.6}Ni_{0.1}Co_{0.1}O_2$ increases the electrolyte penetration, whereas the nanoparticles reduce the lithium ion diffusion path length, thus resulting in the enhancement of electrochemical performance. A combination of XRD, Raman spectra and HRTEM shows that the compound is a solid solution of rhombohedral ($R\bar{3}m$) and monoclinic ($C2/m$) structures. This is yet another advantage, as the monoclinic $C2/m$ symmetry also contributes to the capacity of $Li_{1.2}Mn_{0.6}Ni_{0.1}Co_{0.1}O_2$ by way of activating the Li_2MnO_3 region, especially at 4.4 V, thus reaping the synergistic advantage of being a hybrid electrode material. Cyclic voltammetry and dQ/dV profile exhibit the significant role of synergistic advantages of micro and nanostructure and the activated Li_2MnO_3 region in enhancing the electrochemical properties. This newly developed cathode material delivers a discharge capacity of 242 mA h g^{-1} with an exceptional coulombic efficiency of 97%. The remarkable high capacity and coulombic efficiency could be ascribed to the unique structural, compositional and morphological arrangements found in the $Li_{1.2}Mn_{0.6}Ni_{0.1}Co_{0.1}O_2$ framework and the high voltage activation of Li_2MnO_3 region during cycling. The study reports for the first time about the existence and possible synthesis of novel $Li_{1.2}Mn_{0.6}Ni_{0.1}Co_{0.1}O_2$ cathode with high capacity and excellent coulombic efficiency advantages.

Acknowledgements

Among the authors, P. Remith acknowledges the Department of Science and Technology for the DST-INSPIRE Fellowship and N. Kalaiselvi is grateful to Council of Scientific and Industrial Research (CSIR) for financial support through TAPSUN and MULTIFUN programs. We thank Mr. Prabhu Vijayakumar and Mr. J. Kennedy of CSIR- CECRI for FESEM characterizations, Mr. A. Rathish Kumar of CSIR- CECRI for TEM characterization and Dr. Divesh N. Srivastava and Mr. Gopala Ram Bhadu of CSIR- CSMCRI for HRTEM characterization. Dr. Anuradha Ashok of PSG Institute of Advanced Studies is acknowledged for her timely support in recording the HRTEM images.

Notes

[a] Electrochemical Power Sources Division,
CSIR- Central Electrochemical Research Institute,
Karaikudi- 630006, India
E-mail: kalaiselvicecri@gmail.com

† Electronic Supplementary Information (ESI) available: Fig. S1 represents the STEM elemental mapping of pristine $Li_{1.2}Mn_{0.6}Ni_{0.1}Co_{0.1}O_2$. Fig. S2 is the EDX spectrum obtained from HRTEM and Fig. S3 is the SAED Pattern. Fig. S4 shows the room temperature conductivity plot and Fig. S5 shows the comparison of discharge capacity values of $LiMn_{1/3}Ni_{1/3}Co_{1/3}O_2$ and $Li_{1.2}Mn_{0.6}Ni_{0.1}Co_{0.1}O_2$ cathodes and Table 1 shows the d spacing values corresponding to different space group symmetries, derived from XRD and TEM studies. See DOI: 10.1039/b000000x/

References

1 J. M. Tarascon, M. Armand, *Nature* 2001, **414**, 359-367.
2 M. Armand, J. M. Tarascon, *Nature* 2008, **451**, 652-657.
3 J. B. Goodenough, Y. Kim, *Chem. Mater.* 2010, **22**, 587-603.
4 M. V. Reddy, G. V. Subba Rao, and B. V. R. Chowdari, *Chem. Rev*. 2013, **113**, 5364−5457.
5 C. Masquelier, L. Croguennec, *Chem. Rev.*, 2013, **113**, 6552–6591.
6 L. Zhao, Y. S. Hu, H. Li, Z. Wang, L. Chen, *Adv. Mater*. 2011, **23**, 1385-1388.
7 C. Ban, Z. Li, Z. Wu, M. J. Kirkham, L. Chen, Y. S. Jung, E. A. Payzant, Y. Yan, M. S. Whittingham, A. C. Dillon, *Adv. Energy Mater.* 2011, **1**, 58-62.
8 A. Rougier, P. Gravereau, C. Delmas, *J. Electrochem. Soc.* 1996, **143**, 1168-1175.
9 A. R. Armstrong, A. J. Paterson, A. D. Robertson, P. G. Bruce, *Chem. Mater.* 2002, **14**, 710-719.
10 H. Yu, H. Zhou, *J. Phys. Chem. Lett.* 2013, **4**, 1268-1280.
11 M. M. Thackeray, S. H. Kang, C. S. Johnson, J T. Vaughey, R. Benedek, S. A. Hackney, *J. Mater. Chem.* 2007, **17**, 3112-3125.
12 H. Yu, R. Ishikawa, Y. G. So, N. Shibata, T. Kudo, H. Zhou, Y. Ikuhara, *Angew. Chem. Int. Ed.* 2013, **52**, 5969-5973.
13 N. Yabuuchi, K. Yoshii, S. T. Myung, I. Nakai, S. Komaba, *J. Am. Chem. Soc.* 2011, **133**, 4404-4419.
14 S. Qiu, Z. Chen, F. Pei, F. Wu, Y. Wu, X. Ai, H. Yang. Y. Cao, *Eur. J. Inorg. Chem.* 2013, **16**, 2887-2892.
15 B. Song, M. O. Lai, Z. Liu, H. Liu, L. Lu, *J. Mater. Chem. A* 2013, **1**, 9954-9965.
16 J. Liu, B. Reeja-Jayan, A. Manthiram, *J. Phys. Chem. C* 2010, **114**, 9528-9533.
17 Y. Jiang, Z. Yang, W. Luo, X. Hu, Y. Huang, *Phys. Chem. Chem. Phys.* 2013, **15**, 2954-2960.
18 Y. G. Guo, J. S. Hu, L. J. Wan, *Adv. Mater*. 2008, **20**, 2878-2887.
19 Y. Wang, G. Cao, *Adv. Mater.* 2008, **20**, 2251-2269.
20 P. G. Bruce, B. Scrosati, J. M. Tarascon, *Angew. Chem. Int. Ed.* 2008, **47**, 2930-2946.
21 F. Jiao, Peter G. Bruce, *Adv. Mater.* 2007, **19**, 657-660.
22 X. W. Lou, Y. Wang, C. Yuan, J. Y. Lee, L. A. Archer, *Adv. Mater.* 2006, **18**, 2325-2329.
23 O. Delmer, P. Balaya, L. Kienle, J. Maier, *Adv. Mater*. 2008, **20**, 501-505.
24 A. V. D. Ven, J. Bhattacharya, A. A. Belak. *Acc. Chem. Res*. 2013, **46**, 1216-1225.
25 H. B. Wu, A. Pan, H. H. Hng, X. W. Lou, *Adv. Funct. Mater.* 2013, **23**, 5669-5674.
26 X. Lai, J. E. Halpert, D. Wang, *Energ Environ. Sci.* 2012, **5**, 5604-5618.
27 J. Zhao, Z. Tao, J. Liang, J. Chen, *Cryst. Growth Des*. 2008, **8**, 2799-2805.
28 J. B. Fei, Y. Cui, X. H. Yan, W. Qi, Y. Yang, K. W. Wang, Q. He, J. B. Li, *Adv. Mater.* 2008, **20**, 452-456.
29 Y. D. Yin, R. M. Rioux, C. K. Erdonmez, S. Hughes, G. A. Somorjai, A. P. Alivisatos. *Science* 2004, **304**, 711-714.
30 B. Liu, H. C. Zeng, *Small* 2005, **1**, 566-571.
31 Y. Xiong, B. Wiley, J. Chen, Z. Y. Li, Y. Lin, Y. Xia, *Angew. Chem. Int. Ed.* 2005, **44**, 7913-7917.
32 J. Cao, Y. Zhu, K. Bao, L. Shi, S. Liu, Y. Qian, *J. Phys. Chem. C* 2009, **113**, 17755-17760.
33 X. Zhao, M. V. Reddy, Hanxing Liu, G. V. Subba Rao, B. V. R. Chowdari, *RSC Adv*. 2014, **4**, 24538-24543.
34 M. V. Reddy, G. V. Subba Rao, B. V. R. Chowdari, *J. Power Sources* 2006, **159**, 263-267
35 C. S. Johnson, N. Li, C. Lefief , J. T. Vaughey, M. M. Thackeray, *Chem. Mater.* 2008, **20**, 6095-6106.
36 M. M. Thackeray, S. H. Kang, C. S Johnson, J. T. Vaughey, S. A. Hackney, *Electrochem. Commun*. 2006, **8**, 1531-1538.
37 K. A. Jarvis, Z. Deng, L. F. Allard, A. Manthiram, P. J. Ferreira, *Chem. Mater.* 2011, **23**, 3614-3621.
38 H. J. Yu, H. J. Kim, Y. R. Wang, P. He, D. Asakura, Y. Nakamura, H. S. Zhou, *Phys. Chem. Chem. Phys*. 2012, **14**, 6584-6595.
39 D. Y.W. Yu, K. Yanagida, *J. Electrochem. Soc.* 2011, **158**, A1015-A1022.
40 E. J. W. Verwey, P. B. Braun, E. W. Gorter, F. C. Romeijn, J. H. Van Santen, Z. *Phys. Chem*. 1951, **198**, 6-22.
41 A. R. Armstrong, M. Holzapfel, P. Novák, C. S. Johnson, S-H. Kang, M. M. Thackeray, P. G. Bruce, *J. Am. Chem. Soc*. 2006, **128**, 8694-8698.
42 J. Rana, M. Stan, R. Kloepsch, J. Li, G. Schumacher, E. Welter, I. Zizak, J. Banhart , M. Winter, *Adv. Energy Mater*. 2014, **4**, 1300998 (1-12).
43 M. Gu, I. Belharouak, J. Zheng, H. Wu, J. Xiao, A. Genc, K. Amine, S. Thevuthasan, D. R. Baer, J-G Zhang, N. D. Browning, J. Liu, C. Wang, *ACS Nano* 2013, **7**, 760-767.
44 X. Yu, Y. Lyu, L. Gu, H. Wu, S-M. Bak, Y. Zhou, K. Amine, S. N. Ehrlich, H. Li, K-W. Nam, X-Q. Yang, *Adv. Energy Mater*. 2013, **4**, 1300950 (1-11)